ADVANCED PHOTONICS RESEARCH
Open Access
www.adpr-journal.com

Precise Control of Broadband Light Absorption and Density of Ti^{3+} States in Sputtered Black TiO_2 Thin Films

Dennis Berends, Dereje H. Taffa, Hosni Meddeb, Patrick Schwager, Kai Gehrke, Martin Vehse, and Carsten Agert*

Defect-rich black titanium dioxide (B-TiO_2) has been extensively studied over the past decade due to its enhanced photoelectrochemical efficiency compared to titanium dioxide (TiO_2), which is known for its outstanding photocatalytic stability. So far, most of the B-TiO_2 material is obtained by hydrogenation of crystalline TiO_2, resulting in a disordered outer layer of a few nanometers thickness. Recently, a new sputtering process has been introduced to produce B-TiO_2 thin films without the usage of hydrogen. Herein, the influence of the sputtering process on the creation of Ti^{3+} defect states within the films is discussed. Comprehensive optical, structural, and electronic studies of the thin film suggest that increasing the density of Ti^{3+} states enhances the conductivity of the films and results in increased and broadband light absorption. In addition, the new sputtering method can also be used to alter the density of the defect states in the film in a controlled manner, allowing the optical and electronical properties of the thin film to be changed in a precise and controllable way.

1. Introduction

Thin films of titanium dioxide (TiO_2) are attractive for various modern applications, of which photocatalytic processes are among one of them. The thin films can be prepared in many different ways, for example, reactive sputtering, ultrasonic spray pyrolysis, sol–gel process, electrochemical deposition processes, or pulsed laser deposition.[1–4] The number of possible photocatalytic processes is at least as large as the number of possible deposition methods. TiO_2 has been widely used for reduction of carbon dioxide (preventing or reducing the climate change), water purification (increasing the amount of drinkable water), and water splitting for hydrogen production (long-term storage of energy).[5–10] However, due to its wide bandgap of 3.3 eV, using stochiometric TiO_2 for these processes results in low photocatalytic efficiencies. By increasing the spectral absorptivity of the material, the efficiency of the respective photoelectrochemical process can be increased. Generally, this is done by reducing the bandgap, either by doping with additional elements like carbon, vanadium, iron or by self-doping, where defect states within the bandgap are introduced.[11] Depending on the types of deposition methods and the amount of defect states present, the optical absorption and thus the color of TiO_2 change. When the density of defects is high enough, the layer turns black and shows broadband absorption.[12] Chen et al. were the first to report a synthetic approach to prepare defect-rich black TiO_2 (B-TiO_2). Through hydrogenation of TiO_2 nanoparticles in a high-pressure hydrogen atmosphere, the outer layer became disordered and turned black, resulting in a so-called core–shell particle. Since then, the interest in B-TiO_2 has increased and several different methods for the preparation of black TiO_2 have been published.[13–17] One of the most common methods to create these defects is the controlled treatment of TiO_2 in a reducing atmosphere, for example, hydrogen plasma or annealing in hydrogen gas.[18–20] Only a few reports have demonstrated the creation of defect-rich B-TiO_2 without the use of hydrogen, for example, by reactive sputtering of substoichiometric TiO_x layers.[9,21] Moreover, several applications have been identified where B-TiO_2 shows an increased efficiency compared to TiO_2, for example, photoelectrochemical water splitting, carbon dioxide reduction, water purifications, or cancer treatment.[8,16,22,23] In black TiO_2 free charge carriers occur mainly through Ti^{3+} states. These states are considered to influence the catalytic behavior of the material during photoelectrochemical reactions. Thereby, an increase in the Ti^{3+} states correlates with an increase in reactivity and efficiency.[24,25] Controlling the amount of these states is therefore of great interest. To our knowledge there are no other reports that show precise control of the Ti^{3+} density via a single process parameter during deposition.

In this study, we demonstrate a bipolar reactive sputtering method of B-TiO_2 and show that the absorption and the amount

D. Berends, H. Meddeb, P. Schwager, K. Gehrke, M. Vehse, C. Agert
Urban and Residential Technologies
DLR Institute of Networked Energy Systems
26129 Oldenburg, Germany
E-mail: dennis.berends@dlr.de

D. H. Taffa
Chemical Technology 1
Institute of Chemistry
Carl von Ossietzky Universität Oldenburg
26129 Oldenburg, Germany

The ORCID identification number(s) for the author(s) of this article can be found under https://doi.org/10.1002/adpr.202300163.

DOI: 10.1002/adpr.202300163

of Ti^{3+} states can be precisely adjusted. The process does not require hydrogen and only one sputtering parameter is changed. The sputtering process is driven within oxygen hysteresis, resulting in substoichiometric thin films. The samples are characterized by UV–vis spectrophotometry, X-ray photoelectron spectroscopy (XPS), and X-ray diffraction (XRD) measurements. To investigate the band structure of the samples, the O'Leary-Johnson-Lim (OJL) and the extended Drude model are fit to the measured transmission and reflection data.[26] The results show that the increase of the free charge carrier occurs through the formation of defect states within the bandgap, leading to a new valence band maximum (VBM) and an increased penetration of the band tails into the bandgap.

2. Results & Discussion

As described in more detail in Experimental Section, the power distribution (duty cycle, DC) between the two metallic titanium targets gradually increased, from 71% to 83%. The optical absorption spectra ($A = 1-T-R$) as well as the measured transmission and reflection spectra of the samples prepared with increasing DC are shown in **Figure 1**.

It can be seen that the transmission decreases steadily with increasing DC (Figure 1b). The reflection (Figure 1a), in contrast, shows two regimes. At lower wavelengths (up to 800 nm), the reflection decreases as well. Above 800 nm, however, the reflection increases again. The following experiments indicate that the layer properties change from an isolator-like into a metallic-like material with increasing DC, although neither a pure isolator or metal layer is produced by this inhomogeneous process. This was also confirmed by our previous study.[9] From Figure 1c, it can be seen that the broadband absorption becomes more pronounced with increasing DC. The peaks around 450 nm can thereby directly be related toward defect states inside the thin film.[27] However, for the sample sputtered at 79% DC, the absorption starts to slightly decrease again for wavelength $\lambda > 800$ nm. Here, the increased reflection due to the metallic behavior of the layer gets more dominant, which also explains the broadening of the peak around 450 nm. For DC > 81%, no change in the optical properties can be observed. This can be seen as the curves for the 81% and 83% DC samples overlap. In addition, it can be seen in Figure 1 that the pure TiO_2 sample absorbs only at wavelengths below 380 nm.

The bandgap of the pristine TiO_2 sample, as calculated by the OJL model, is $E_g = 3.51 \pm 0.02$ eV. This is in good agreement with literature.[28,29] The bandgap values of the samples sputtered within the low-oxygen regime remain almost the same (3.54 ± 0.03 eV). It can be concluded that the band edges (without defect tail states) remain fixed and the increased absorption may have another reason. To gain further insight into the structure of the samples, we studied their crystal phases. The XRD measurements of the samples along with images of the respective samples are shown in **Figure 2**.

Figure 2 shows that the color of the B-TiO_2 changes as DC increases. While the TiO_2 sample (Figure 2 bottom row) is transparent, the nonstoichiometric sample sputtered at 71% DC has a purple color. With increasing DC, the color changes from blue to black. The XRD measurements for the TiO_2 sample indicate a dominant anatase crystal structure (Figure 2, highlighted in green). Being within the oxygen hysteresis, the sample sputtered at 71% DC exhibits a mixture of anatase and rutile structures, as indicated by the XRD measurement. However, the intensity of the rutile phase increases drastically at 71% DC compared to the TiO_2 sample and decreases again until 75% DC. This behavior can be explained by the increased amount of titanium inside the layer, as shown in our previous publication.[9] Through this

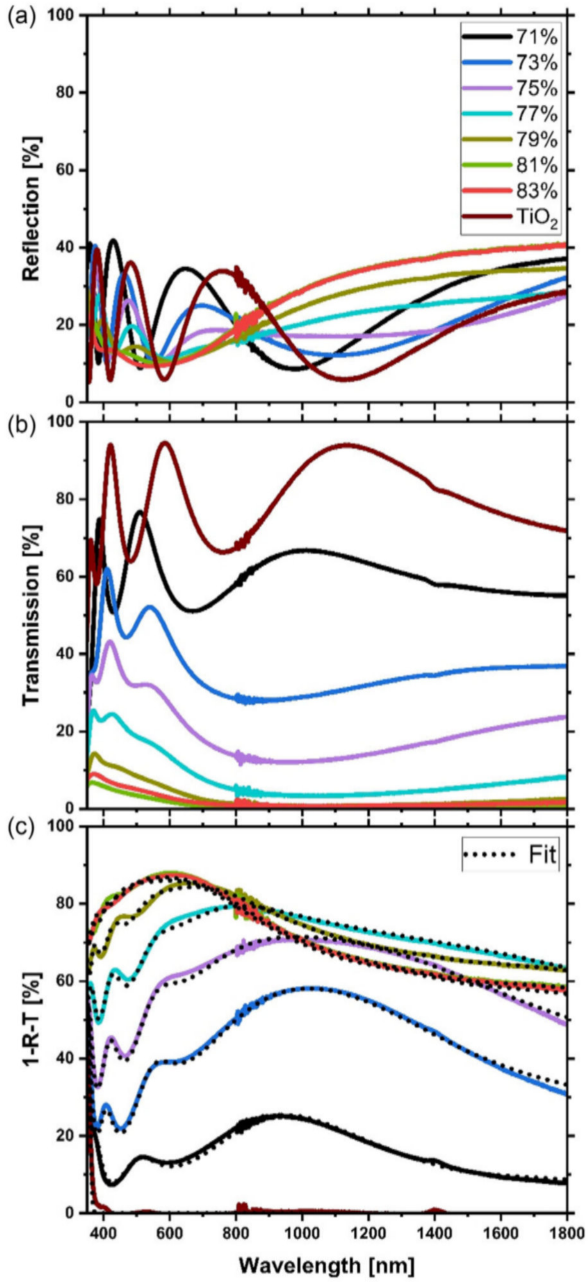

Figure 1. a) Reflection and b) transmission curves of the samples. c) Absorption ($1-R-T$) measurement and corresponding fits of the respective samples. For better illustration, only every second DC is displayed. The black dots represent the fitted curves of the corresponding measured values (solid line).

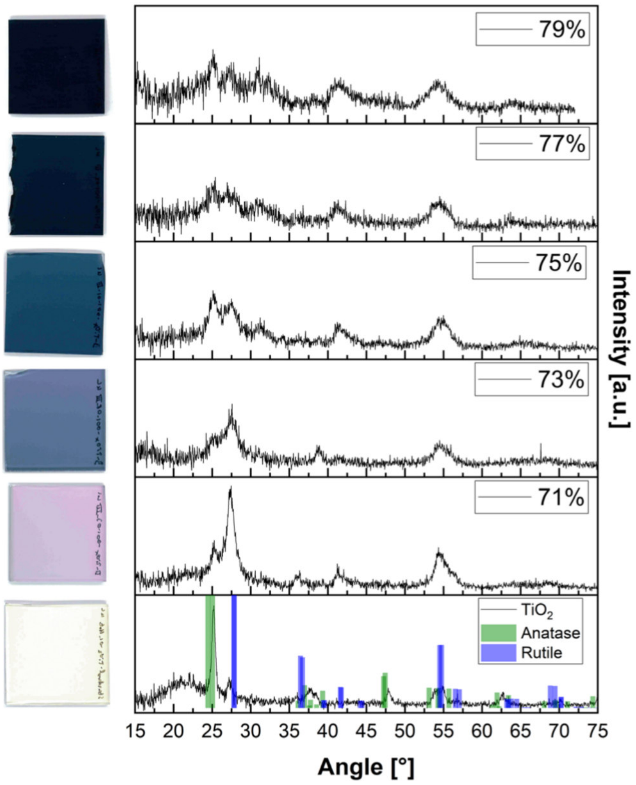

Figure 2. Left: Images of the samples corresponding to the XRD measurement. Right: XRD measurements of the samples. In the bottom row, theoretical values for anatase (ICDD reference code: 00-021-1272) and rutile (ICDD reference code: 00-016-0934) peaks are shown.

additional implementation, the thin films become more dense which promotes rutile phases above anatase phases.[30] Increasing the DC further broadens the main peaks. At 77% DC, only some small rutile peaks with no anatase structures can be seen. The samples do not exhibit a dominant crystal structure and seem to be amorphous.[31] The further increase of titanium atoms in the layer disturbs the formation of crystal structures.

To get more insight into the morphology of the samples, SEM measurements were done. For selected samples, these images are shown in **Figure 3**.

From the SEM images in Figure 3 it can be concluded that the samples consist of grains in the submicrometer range. With increasing DC the size of the grains decreases, which is supported by the decreasing intensity of the XRD peaks, as shown in Figure 2.

To understand the increasing of absorption shown in Figure 1, the plasma frequency for each sample has been calculated using the Drude–Lorentz model. In addition, XPS measurements were performed and the ratio of the peak area of Ti^{3+} to Ti^{4+} states was calculated. The Ti^{3+} states can be associated with defects formed inside the bandgap.[32] Furthermore, the dark conductivity of the samples was measured. The results are presented in **Figure 4**.

The Ti 2*p* XPS envelope spectra of the samples are shown in Figure 4a. For each peak, the Ti^{3+} and Ti^{4+} states were fit, exemplarily shown in Figure 4b. No Ti^{3+} states were detected for the TiO_2 sample, which correlates with the absence of defects, and therefore no plasma frequency could be calculated.[33] With increasing DC, the Ti^{3+} peak centered at 457 eV increases. The ratio of the peak areas of the Ti^{3+} states to the Ti^{4+} states confirms this trend (Figure 4c). At 75% DC the ratio converges. However, as the DC increases, the plasma frequency increases until 76% DC, where it reaches saturation, supporting the trend as seen for the amount of free charge carriers. However, the dark conductivity in Figure 4d shows an exponential increase whereas the crystal size decreases (as shown in Figure 3) for increasing DCs, as shown in Figure 3. To understand this phenomenon of increasing absorption shown in Figure 1; especially for samples

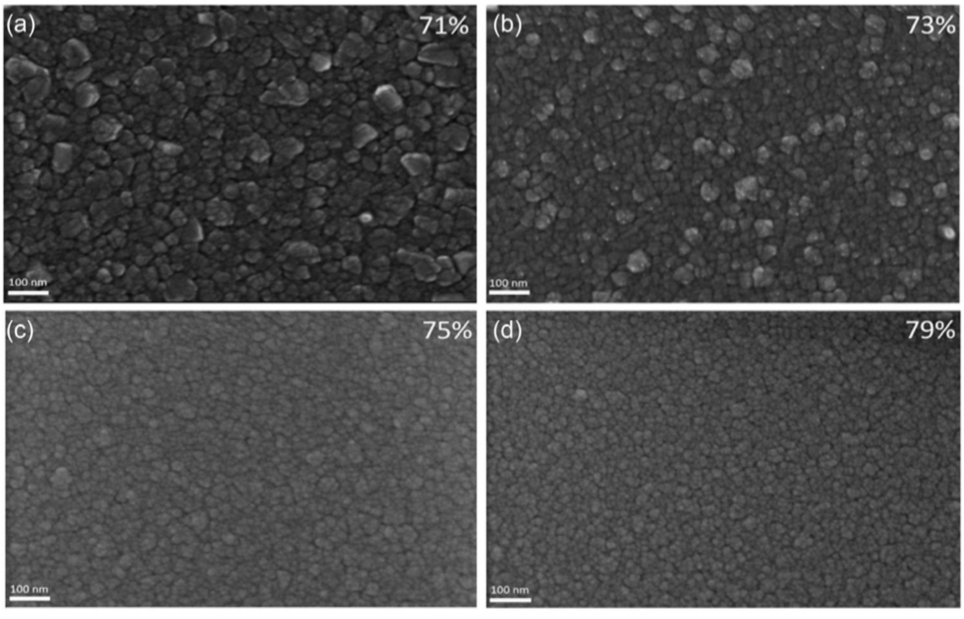

Figure 3. SEM images of the sputtered samples, taken at 100 k magnification. a) 71% DC; b) 73% DC; c): 75% DC; d) 79% DC.

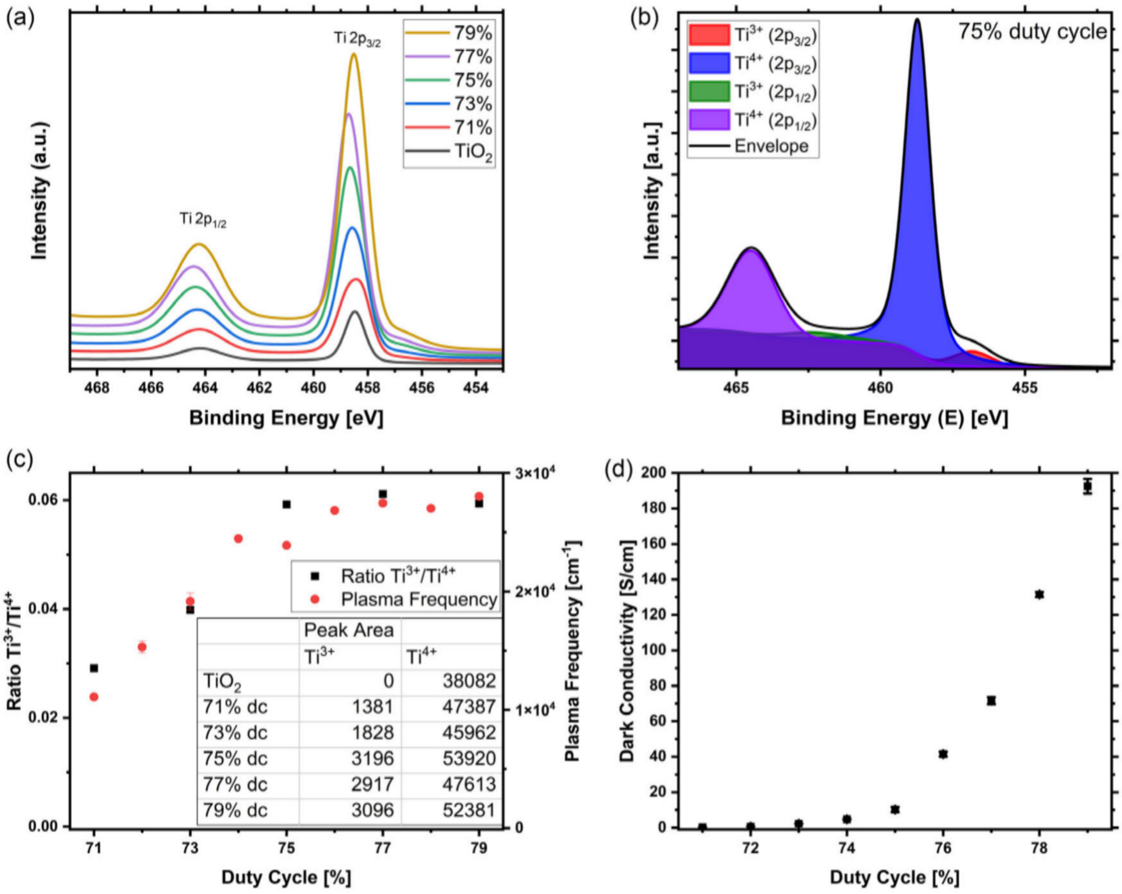

	Peak Area	
	Ti^{3+}	Ti^{4+}
TiO_2	0	38082
71% dc	1381	47387
73% dc	1828	45962
75% dc	3196	53920
77% dc	2917	47613
79% dc	3096	52381

Figure 4. a) XPS measurements of the Ti 2*p* spectra; b) fitting of the Ti^{3+} and Ti^{4+} states to the corresponding peaks, exemplarily shown for the sample sputtered at 75% DC; c) ratio of the Ti^{3+} and Ti^{4+} states of the investigated samples, derived from the fitted peak area (inserted table) of the XPS measurements (black) and the plasma frequency of the samples calculated through the Drude–Lorentz model with error given by the software (red); d) dark conductivity of all samples.

with a DC of more than 75%, the OJL model must be studied in more detail. Since the number of defect states does not continue to increase with higher DC, as shown in Figure 4c, the damping constant calculated with the gamma function γ must be considered first. The gamma function of the OJL model is helpful to describe the tail states that enter the bandgap. A decreasing value reflects a decreasing distance between the band tails.[34] The value of this function is shown in **Figure 5**.

The plot of the gamma function from the OJL model shows that the samples between 71% and 75% DC have an increased amount of band tail states compared to the TiO_2 sample ($1025\ cm^{-1}$, not shown). These samples were sputtered within the oxygen hysteresis and are therefore defect rich as expected.[35] A further decreasing gamma function for samples above 75% DC can also be seen. As the DC increases, the band tail states penetrate deeper into the bandgap even though the number of defects is saturated. For samples sputtered with a DC of more than 79%, the gamma function value saturates (not shown). Different kinds of defect states inside the bandgap can be the reason for the increased tail states and thus provide the explanation for the increased absorption and dark conductivity of the samples. In another study, the influence of the different degrees of localization was investigated.[36] Di Valentin et al. claimed that different defect states are created within the bandgap depending on localization. While the amount of Ti^{3+} states remains, their

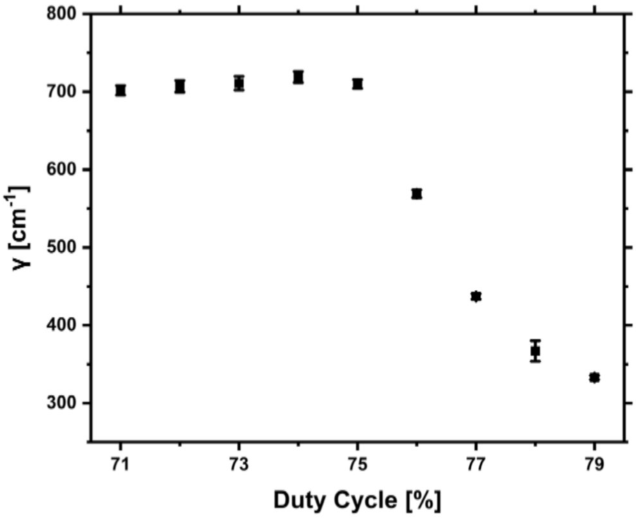

Figure 5. Gamma function, derived from the OJL model.

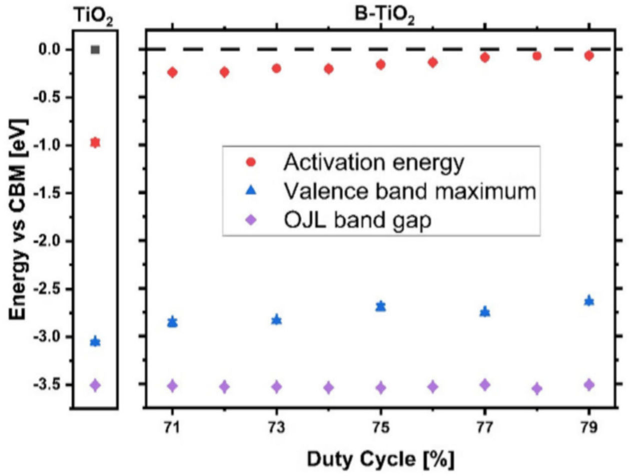

Figure 6. VBM, activation energy, and bandgap (derived by the OJL model) of the samples relative to the CBM (set to 0 eV).

localization can change, giving the explanation for the increased band tail states. However, the bandgap derived by the OJL model does not consider these tail states. Therefore, the VBM was determined by XPS measurements and can be related to the conduction band minimum (CBM). **Figure 6** shows the VBM, the activation energy, and the calculated bandgap of the OJL model in relation to the CBM (set at 0 eV).

It should be noted that the VBM refers to the Fermi level of the corresponding sample.[37] Therefore, dark conductivity measurements were performed to calculate the activation energy. It indicates the Fermi level relative to the conduction band. The activation energy of our TiO$_2$ sample is in good agreement with reported literature.[38] In addition, a clear decrease in the activation energy from 0.97 eV for the TiO$_2$ sample toward 0.24 eV for the sample sputtered at 71% DC can be observed. With further increase of the DC, a decrease in the activation energy can be seen. Above 77% DC, the values tend to saturate.

For the TiO$_2$ sample, the bandgap energies given by the difference of CBM and VBM and by the OJL model show a small offset. The OJL model calculates the bandgap without the presence of the band tails. However, band tails were calculated for this sample by the Drude model. Therefore, the bandgap derived from the VBM measurement is lower than what was calculated with the OJL model, as the band tails are considered at the former method. The difference between CBM and VBM slightly decreases for the samples prepared at different DCs and at 16×10^{-6} mbar oxygen partial pressure, although it is significantly smaller than the VBM for the TiO$_2$ sample. Tan et al. reported a change in the crystalline structure from anatase-to-rutile phase with the VBM rising of about 1.0–1.5 eV.[39] The crystal structure of the samples shown here exhibits a similar change as indicated by the XRD measurements in Figure 2.

3. Conclusion

A systematic analysis of the structural, optical, and electrical properties of black TiO$_2$ samples prepared by a modified bipolar reactive magnetron sputtering technique was performed. It was demonstrated that the absorption of B-TiO$_2$ can be precisely changed by varying only the power distribution between the two titanium targets. These findings provide further insights into the properties of sputtered black TiO$_2$ thin films without hydrogen treatment and without a core–shell structure. Fitting of the optical data with different models suggests that the density of the Ti^{3+} states can be modified in a controlled manner up to a certain duty cycle. Above this duty cycle, the width of the tail states within the bandgap increases, explaining the increased absorption and enhanced dark conductivity. Furthermore, the reduced bandgap can help to fabricate a material suitable for various applications, for example, tandem photoelectrochemical cells. In addition, the catalytic efficiency of many different reactions can be improved through the controlled implementation of the Ti^{3+} states. It can also be assumed that, on the one hand, a change of the oxygen partial pressure shifts the position of the duty cycle at which the maximum of Ti^{3+} states are reached. On the other hand, a lower oxygen partial pressure can lead to a further decreased bandgap and thus increase the variability of the black TiO$_2$.

4. Experimental Section

Sample Preparation: The samples were prepared by closed-loop reactive bipolar magnetron sputtering using the in-line vacuum system Vistaris 600 (Singulus Technologies AG, Germany). Two cylindrical titanium targets (purity 3 N) with a length of 600 mm and a diameter of 155 mm were used. The total power of 8 kW was distributed between the two targets from 71% toward 83% DC to deposit samples (10 × 10 cm) with varying defect density. Through closed feedback control, the oxygen flow was kept inside the oxygen hysteresis, resulting in a constant oxygen partial pressure and in nonstoichiometric films. A detailed description of the process can be found in the study by Berends et al.[9] The produced layer thicknesses was in the range of 240–270 nm. For the electrical measurements, two 1 × 1 cm^2 silver contacts were deposited on top of the via electron beam evaporation (VTD Vakuumtechnik Dresden GmbH, Germany). An area of 0.1 × 1 cm was left uncoated in the middle of the two silver contacts.

Characterization Methods: Transmission (T) and reflection (R) measurements were carried out in a Cary 5000 UV–vis–NIR spectrophotometer using an integrating sphere (Agilent Technologies Inc., USA) in the wavelength range from 300 to 2000 nm. The thickness (d) of the deposited films was measured using a Dektak 150 stylus profilometer (Veeco, USA). The thin-film optic software CODE/Scout (WTheiss Hardware and Software, USA), which uses the 1D transfer matrix method, was used to create optical models of the samples, using transmission and reflection measurements. The OJL model as well as the Drude–Lorentz model were chosen in the software. The OJL model describes the bandgap transition using the bandgap energy $E_{g,\,OJL}$ as well as a parameter to account for the exponential tail γ penetrating into the bandgap.[26] The Drude–Lorentz model allows for calculating the plasma frequency ω_p using the free-electron density n_e, for example, $\omega_p = \sqrt{n_e e^2 / m_e \varepsilon_0}$. This parameter represents the density of defect states in the thin film. The remaining parameters describe the electron charge e, the material related effective electron mass m_e, and the vacuum permittivity ε_0.[40]

Chemical state (oxidation state) analysis was performed through XPS measurements in an ultrahigh-vacuum setup. The ESCALAB 250 Xi (Thermo-Fisher, UK) was equipped with a monochromatic Al Kα X-ray source ($h\nu = 1486.6$ eV). High-resolution spectra were recorded for the C 1s, O 1s, N 1s, and Ti 2p photoelectron lines. A pass energy of 10 eV and a step size of 0.02 eV was chosen. Valence band XPS spectra were measured at a pass energy of 20 eV with an energy resolution of 0.05 eV. The binding energy scales were calibrated to the most intense

C 1*s* peak at 284.8 eV. The Avantage software (version 5.9925, Thermo Fisher Scientific, USA) was used to analyze the spectra.

Dark conductivity (σ_d) measurements were performed using the two-point probe technique. A constant bias voltage of 5 V was applied, and the current was measured using a Keithley 2636 A (Keithley Instruments, USA). The samples were heated in vacuum up to a temperature T of 120 °C and then passively cooled to 50 °C. The temperature was measured with a Pt100 probe. According to the Petritz model, the dark conductivity can be calculated using the relation $\sigma_d = \sigma_0 \exp(-E_a k^{-1} T^{-1})$, where σ_0 is a constant, k the Boltzmann constant, and E_a the activation energy.[41] The activation energy contributed to localized states close to the Fermi level.[42]

To get insights of the crystal structures and phase composition of the samples, grazing-incident X-ray diffractograms measurements were performed with a PANalaytical Empyrean diffractometer (Malvern PANalytical, Netherlands) with CuKα = 1.54 Å radiation at an incident angle of 0.2°. The diffractograms were recorded over a range of $2\Theta = 15°–80°$.

To create images of the sample, a Zeiss Neon 40 EsB crossbeam scanning electron microscope (Carl Zeiss Ag, Germany) was used.

Acknowledgements

The authors thank M. Götz-Köhler, N. Ostherthun, U. Banik, and L. Busch for fruitful discussion and supporting this publication.

Open Access funding enabled and organized by Projekt DEAL.

Conflict of Interest

The authors declare no conflict of interest.

Data Availability Statement

The data that support the findings of this study are available from the corresponding author upon reasonable request.

Keywords

bipolar sputtering of thin films, black titanium dioxide, optical modeling

Received: May 20, 2023
Revised: August 10, 2023
Published online:

---

[1] A. Brudnik, A. Gorzkowska-Sobaś, E. Pamuła, M. Radecka, K. Zakrzewska, *J. Power Sources* **2007**, *173*, 774.

[2] H. Ennaceri, M. Boujnah, A. Taleb, A. Khaldoun, R. Sáez-Araoz, A. Ennaoui, A. El Kenz, A. Benyoussef, *Int. J. Hydrogen Energy* **2017**, *42*, 19467.

[3] S. Shen, J. Chen, M. Wang, X. Sheng, X. Chen, X. Feng, S. S. Mao, *Prog. Mater. Sci.* **2018**, *98*, 299.

[4] N. Saranrom, T. Sintiam, R. Panyathip, K. Hongsith, S. Sucharitakul, A. Ngamjarurojana, D. Boonyawan, P. Kumnorkaew, T. Kerdcharoen, S. Choopun, *Phys. Status Solidi A* **2021**, *218*, 2000239.

[5] J. Nowotny, T. Bak, M. Nowotny, L. Sheppard, *Int. J. Hydrogen Energy* **2007**, *32*, 2609.

[6] O. Ola, M. Maroto-Valer, *J. Photochem. Photobiol. C* **2015**, *24*, 16.

[7] K. Perović, F. M. dela Rosa, M. Kovačić, H. Kušić, U. Lavrenčič Štangar, F. Fresno, D. D. Dionysiou, A. L. Bozic, *Materials* **2020**, *13*, 1338.

[8] A. Chatzitakis, S. Sartori, *ChemPhysChem* **2019**, *20*, 1272.

[9] D. Berends, P. Schwager, K. Gehrke, M. Vehse, C. Agert, *Vacuum* **2022**, *203*, 111290.

[10] K. Zhang, L. Wang, J. K. Kim, M. Ma, G. Veerappan, C.-L. Lee, K. Kong, H. Lee, J. H. Park, *Energy Environ. Sci.* **2016**, *9*, 499.

[11] S. Kim, Y. Cho, R. Rhee, J. H. Park, *Carbon Energy* **2020**, *2*, 44.

[12] A. Naldoni, M. Altomare, G. Zoppellaro, N. Liu, S. Kment, R. Zboril, P. Schmuki, *ACS Catal.* **2019**, *9*, 345.

[13] X. Chen, L. Liu, P. Y. Yu, S. S. Mao, *Science* **2011**, *331*, 746.

[14] X. Chen, L. Liu, F. Huang, *Chem. Soc. Rev.* **2015**, *44*, 1861.

[15] X. Liu, G. Zhu, X. Wang, X. Yuan, T. Lin, F. Huang, *Adv. Mater.* **2016**, *6*, 1600452.

[16] M. Soleimani, J. B. Ghasemi, A. Badiei, *Inorg. Chem. Commun.* **2022**, *135*, 109092.

[17] K. H. Kim, C.-W. Choi, S. Choung, Y. Cho, S. Kim, C. Oh, K.-S. Lee, C.-L. Lee, K. Zhang, J. W. Han, S. Y. Choi, *Adv. Mater.* **2022**, *12*, 2103495.

[18] G. Feng, M. Hu, S. Yuan, J. Nan, H. Zeng, *Nanomaterials* **2021**, *11*, 2801.

[19] M. Pylnev, W.-H. Chang, M.-S. Wong, *Appl. Surf. Sci.* **2018**, *462*, 285.

[20] X. Yan, Y. Li, T. Xia, *Int. J. Photoenergy* **2017**, *2017*, 8529851.

[21] L. C. Escaliante, A. L. D. J. Pereira, L. J. Affonço, J. H. D. Da Silva, *J. Mater. Res.* **2021**, *36*, 3096.

[22] S. A. Rawool, K. K. Yadav, V. Polshettiwar, *Chem. Sci.* **2021**, *12*, 4267.

[23] W. Ren, Y. Yan, L. Zeng, Z. Shi, A. Gong, P. Schaaf, D. Wang, J. Zhao, B. Zou, H. Yu, G. Chen, *Adv. Healthcare Mater.* **2015**, *4*, 1526.

[24] K. Zhang, J. H. Park, *J. Phys. Chem. Lett.* **2017**, *8*, 199.

[25] J. Jiang, Z. Xing, M. Li, Z. Li, X. Wu, M. Hu, J. Wan, N. Wang, A. S. Besov, W. Zhou, *Ind. Eng. Chem. Res.* **2017**, *56*, 7948.

[26] Z. Qiao, C. Agashe, D. Mergel, *Thin Solid Films* **2006**, *496*, 520.

[27] M. Kitano, M. Takeuchi, M. Matsuoka, J. M. Thomas, M. Anpo, *Chem. Lett.* **2005**, *34*, 616.

[28] J. Aljuaid, A. Timoumi, S. N. Alamri, *Opt. Mater.: X* **2022**, *16*, 100178.

[29] S. K. Mukherjee, D. Mergel, *J. Appl. Phys.* **2013**, *114*, 13501.

[30] M. M. Masayoshi Mikami, S. N. Shinichiro Nakamura, O. K. Osamu Kitao, H. A. Hironori Arakawa, X. G. Xavier Gonze, *Jpn. J. Appl. Phys.* **2000**, *39*, L847.

[31] S. Boukrouh, R. Bensaha, S. Bourgeois, E. Finot, M. C. Marco de Lucas, *Thin Solid Films* **2008**, *516*, 6353.

[32] B. Bharti, S. Kumar, H.-N. Lee, R. Kumar, *Sci. Rep.* **2016**, *6*, 32355.

[33] X. Pan, M.-Q. Yang, X. Fu, N. Zhang, Y.-J. Xu, *Nanoscale* **2013**, *5*, 3601.

[34] J. Boltz, D. Koehl, M. Wuttig, *Surf. Coat. Technol.* **2010**, *205*, 2455.

[35] R. Gouttebaron, D. Cornelissen, R. Snyders, J. P. Dauchot, M. Wautelet, M. Hecq, *Surf. Interface Anal.* **2000**, *30*, 527.

[36] C. Di Valentin, G. Pacchioni, A. Selloni, *J. Phys. Chem. C* **2009**, *113*, 20543.

[37] V. Pfeifer, P. Erhart, S. Li, K. Rachut, J. Morasch, J. Brötz, P. Reckers, T. Mayer, S. Rühle, A. Zaban, I. Mora Sero, *J. Phys. Chem. Lett.* **2013**, *4*, 4182.

[38] K. Pomoni, A. Vomvas, C. Trapalis, *Thin Solid Films* **2008**, *516*, 1271.

[39] H. Tan, Z. Zhao, M. Niu, C. Mao, D. Cao, D. Cheng, P. Feng, Z. Sun, *Nanoscale* **2014**, *6*, 10216.

[40] C. J. Dahlman, A. Agrawal, C. M. Staller, J. Adair, D. J. Milliron, *Chem. Mater.* **2019**, *31*, 502.

[41] W. Rehm, R. Fischer, J. Stuke, H. Wagner, *Phys. Status Solidi B* **1977**, *79*, 539.

[42] A.-M. Lepadatu, A. Slav, C. Palade, I. Dascalescu, M. Enculescu, S. Iftimie, S. Lazanu, V. S. Teodorescu, M. L. Ciurea, T. Stoica, *Sci. Rep.* **2018**, *8*, 4898.